



Geochemistry, Geophysics, Geosystems



RESEARCH ARTICLE

10.1029/2021GC010020

Key Points:

- Seismic waves sampling the northeastern edge of the Pacific Large Low Shear Velocity Province (LLSVP) show strong waveform complexity and rapid change in differential time
- Waveform and mineralogical modeling suggest a magnesiowüstitebearing ultra-low velocity zone adjacent to slab at edge of LLSVP, conducive to plume formation
- The structural anomalies and proposed plume are located ~12° southeast of present-day Hawai'i, in agreement with recent mantle flow models

Supporting Information:

Supporting Information may be found in the online version of this article.

Correspondence to:

V. H. Lai, voonhui.lai@anu.edu.au

Citation:

Lai, V. H., Helmberger, D. V., Dobrosavljevic, V. V., Wu, W., Sun, D., Jackson, J. M., & Gurnis, M. (2022). Strong ULVZ and slab interaction at the northeastern edge of the Pacific LLSVP favors plume generation. *Geochemistry*, *Geophysics*, *Geosystems*, 23, e2021GC010020. https://doi. org/10.1029/2021GC010020

Received 8 JUL 2021 Accepted 29 JAN 2022

© 2022 The Authors. This is an open access article under the terms of the Creative Commons Attribution-NonCommercial License, which permits use, distribution and reproduction in any medium, provided the original work is properly cited and is not used for commercial purposes.

Strong ULVZ and Slab Interaction at the Northeastern Edge of the Pacific LLSVP Favors Plume Generation

Voon Hui Lai^{1,2} , Don V. Helmberger¹, Vasilije V. Dobrosavljevic¹, Wenbo Wu¹, Daoyuan Sun³, Jennifer M. Jackson¹, and Michael Gurnis¹

¹Seismological Laboratory, California Institute of Technology, Pasadena, CA, USA, ²Research School of Earth Sciences, The Australian National University, Acton, ACT, Australia, ³Laboratory of Seismology and Physics of Earth's Interior, School of Earth and Space Sciences, University of Science and Technology of China, Hefei, China

Abstract Strong waveform complexities, including multipathing of the S diffracted phase and rapid changes in differential ScS-S times, are observed for multiple deep Fiji earthquakes recorded at the USArray. The complexities occur at the northeastern edge of the Pacific Large Low Shear Velocity Province (LLSVP), about 12 degrees southeast of present-day Hawai'i. Waveform modeling of the multipathing provides good constraints on an ultra-low velocity zone (ULVZ) with a width of 5 degree located near the inner edge of the LLSVP. Based on the mineralogical-modeling of the ULVZ as a solid iron-rich magnesiowüstite-bearing assemblage with compatible morphology predicted from geodynamical simulations, a ULVZ model with a thickness of 30 km and a shear wave velocity reduction of 18% is preferred. The rapid change in differential ScS-S travel time is best explained by having both the aforementioned ULVZ and an adjacent high velocity structure near the LLSVP. Furthermore, a low-velocity plume-like structure could potentially explain the observed S travel time delay independent of ScS. These seismic features are proposed to be a ULVZ driven toward the edge of the LLSVP while potentially pushed by a subducted slab. This configuration may trigger plume generation due to strong thermal instabilities and is in the same vicinity where mantle flow models place the present-day Hawaiian plume source. Multiple ScS can potentially be used to verify vertical plume structure in tomographic models but the accuracy of upper mantle structure, which is a key reflection point, needs to be considered.

Plain Language Summary Seismic waves from earthquakes in Fiji recorded by seismometers in the United States travel close to the core-mantle boundary (CMB) and can be used to image fine-scale structures along the edge of a previously known large province near the CMB with low seismic wave velocity, namely the Pacific LLSVP. The edges of the Pacific LLSVP are of interest because they contain many structural anomalies, thought to be correlated with hotspots on Earth's surface, including Hawai'i, and can host the plume sources for these hotspots. In this study, we observed two phenomena: (a) seismic waves with an additional unexpected pulse due to the presence of a very low velocity structure and (b) a rapid change in the travel time behavior of two seismic phases which can be explained by the same low velocity structure adjacent to a high velocity structure. We constrained these two structures to be at the edge of the LLSVP, a configuration favorable for generating long-lasting plume, that is, the source for the Hawaiian hotspot. The location of these structures is in agreement with the hypothesized source location from recent geodynamical studies. We also showed that this low velocity structure could be composed of a solid iron-rich material.

1. Introduction

The northeastern margin of the Pacific Large Low Shear Velocity Province (LLSVP) is particularly interesting as many seismic modeling studies have suggested the presence of multiple structural anomalies in this lower-most mantle region. There is a strong velocity change from the interior of the Pacific LLSVP toward the margin, inferred to be a high velocity, post-perovskite lens thins toward the edge while an ultra-low velocity zone (ULVZ) layer increases in thickness (Lay et al., 2006). To et al. (2011) also proposed a localized, slow ULVZ-like anomaly embedded inside or at the margin of the LLSVP from their modeling of the anomalous S and diffracted S (Sdiff) behaviors observed with a limited number of stations.

The deployment of USArray, recording many deep earthquakes from Fiji-Tonga subduction zone, greatly increases the sampling points to study the lateral structural variation along this margin. Through deconvolution

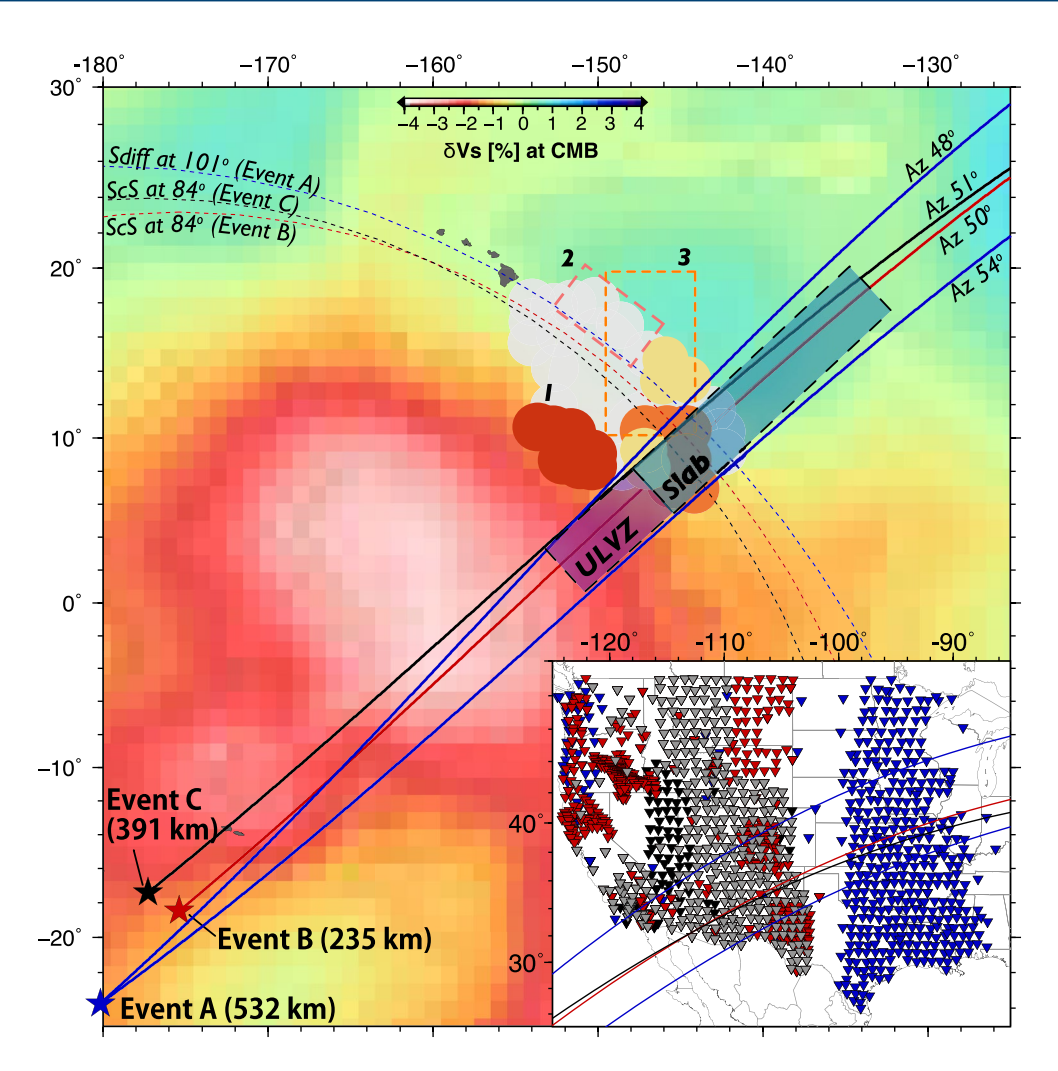


Figure 1. Location of the proposed ultra-low velocity zone-slab structure near the northeastern edge of Pacific Large Low Shear Velocity Province. Map shows the location of the three deep Fiji events, which are Event A (29 July, 2011 Mw6.7 at 532 km depth), Event B (22 October 2008 Mw6.4 at 235 km depth), and Event C (19 July 2008 Mw6.4 at 391 km depth). The background is shear wave perturbation from GyPSuM model (Simmons et al., 2010) at the CMB. The inset shows the stations used in this study, color-coded by events. Stations used for both Event B and C are colored in gray. The color-coded thick lines in the main map and inset show the ray paths sampling the northeastern edge of the Pacific LLSVP, the Sdiff pierce point for Event A at a distance of 101°, and the ScS bounce points for Events B and C at a distance of 84°, estimated using a 1-D IASP model. Group 1 shows the thickness distribution of ULVZ identified in Zhao et al. (2017; Figure 13) where the patches in gray, yellow, orange, and red represent a thickness of <5, 10, 14, and 20 km, respectively. Box 2 marks the location of ULVZ proposed by Sun et al. (2019). Box 3 is the estimated location of present-day plume by Hassan et al. (2016) at the CMB.

and stacking of short period ScS pre- and post-cursor energies, Zhao et al. (2017) proposed this region hosts several clusters of ULVZs with non-uniform thicknesses (<5–20 km) and with a strong velocity reduction (30%) (Figure 1; Group 1). The ULVZ cluster is modeled to be the thickest inside the LLSVP and becomes thinner toward the edge of the LLSVP. Apart from the lateral variation in ULVZ thicknesses, the region toward the edge is thought to be more complex with layers of fast and slow velocity compared to the region with the thickest ULVZ. Jenkins et al. (2021) further expanded on the ScS pre- and post-cursors study by Zhao et al. (2017) and suggested an asymmetric ULVZ ridge, increasing in thickness toward northeast along this margin. Sun et al. (2019) also showed there are strong multipathing of ScS at two distinct patches along this boundary for several earthquakes (Figure S1 and Table S1 in Supporting Information S1). The northern patch (Figure 1, Box 2) is modeled extensively as a ULVZ structure in Sun et al. (2019) and Jenkins et al. (2021).

LAI ET AL. 2 of 19



This location with a strong presence of structural anomalies is geodynamically interesting as it coincides with the proposed plume location rooted within the deep mantle that gives rise to the Hawaii-Emperor seamount chain (Hassan et al., 2016). Geodynamical modeling has attempted to track the evolution of the plume location which needs to fit several features of the Hawaii-Emperor seamount chain, including a relatively sharp bend at 47 Ma, a rapid change in migration rate of volcanic islands, and the formation of individual volcanoes at different paleolatitudes (Tarduno et al., 2009). Although global mantle flow could distort upwelling plumes and may explain the observed hotspot motion (Steinberger et al., 2004), Hassan et al. (2016) argued that the sharp bend and migration rate in Hawaiian hotspot can be partly explained by the migration of the plume source along the core-mantle boundary (CMB). Their mantle flow model showed that the strong and persistent subduction in the north Pacific can influence deep mantle flow, deform the Pacific LLSVP, and cause the southward migration of the Hawaiian plume to its current location at the northeastern edge of the Pacific LLSVP about 12° southeast of Hawai'i (Figure 1, Box 3). However, global tomographic models (e.g., French & Romanowicz, 2015; Zhao, 2004) prefer broad vertical plumslue-like structure directly beneath the Hawaiian hotspot. This apparent mismatch between geodynamical and seismological results warrants new ways to image and model the plume.

Most seismic studies focus on a single wave type, either core-reflected phases (e.g., ScS), core waves (e.g., SPdKS + SKPdS) or diffracted energy (e.g., Sdiff) which samples the CMB differently. Furthermore, these studies use 1-D waveform modeling to attribute observed waveform anomalies to a single type of structure, for example, ULVZ and cannot model waveform interaction due to lateral variation of structural anomalies. However, He and Wen (2012) alluded to a complex interaction of slow and fast structures across the LLSVP margin. In this study, we combine multiple wave types (S, ScS, and Sdiff) covering a wide distance range (75° to 105°) and present seismic evidence for a strong lateral structural variation across the northeastern edge of Pacific LLSVP, particularly along an azimuth corridor centered at ~50° (Figure 1). Based on 2-D waveform-modeling, we hypothesize this rapid variation reflects a complex interaction between a ULVZ in the inner edge of the Pacific LLSVP being impinged by a subducted slab at the outer edge, which can potentially give rise to a plume. In the discussion, we present a solid-state compositional model containing iron-rich (Mg, Fe)O magnesiowüstite that can explain the observed ULVZ properties and address the trade-off between the ULVZ velocity reduction and thickness. The resulting possibility of highly conductive interconnected magnesiowüstite could provide a mechanism for increased bulk thermal conductivity and enhanced plume generation. Finally, we discuss the potential of using vertically-incident ScS and its limitation to image the Hawaiian plume.

2. Observation

We focused on three deep earthquakes from the Fiji-Tonga region, namely Events A, B and C (Figure 1 caption and Table S1 in Supporting Information S1) which sample the northeastern boundary of the Pacific LLSVP centered at N 10°W 145°. These events are chosen because their deep source depths minimize contamination from the depth phases, their source mechanisms have strong SH radiation pattern, and their source time functions are simple. The seismic waveforms shown are tangential displacements, filtered from 5 to 80 s. To increase the signal-to-noise ratio, the data from neighboring stations within 0.75 degree are stacked by aligning the waveform to the expected S arrival time based on the 1-D IASP model (Kennett & Engdahl, 1991).

2.1. Multipathing of Sdiff

Multipathing occurs when a wave front encounters sharp velocity gradients, resulting in multiple close arrivals and waveform distortion. The multipathing can be in-plane or out-of-plane, depending on how the wavefront interacts with the velocity gradients. An example of out-of-plane multipathing is the waveform complexity of SKS and the rapid lateral variation of travel time for Sdiff as these phases sample the edge of the African LLSVP along strike (Ni et al., 2005). The multipath detector (Sun et al., 2009) is subsequently developed to distinguish between the in-plane and out-of-plane multipathing by decomposing the observed pulses within the body wave observation based on diffraction summation and measuring the relative timing of these arrivals.

The Sdiff phases recorded by Event A show strong multipathing, where an additional pulse (S*) arrives within 5 s after the main Sdiff pulse (Figure 2). Following the multipath detector method developed by Sun et al. (2009), we define the multipathing as a summation of the two pulses, where the first pulse ("Sdiff") is the simplest observed waveform representing the empirical source function and the second pulse ("S*") is modulated from the first

LAI ET AL. 3 of 19



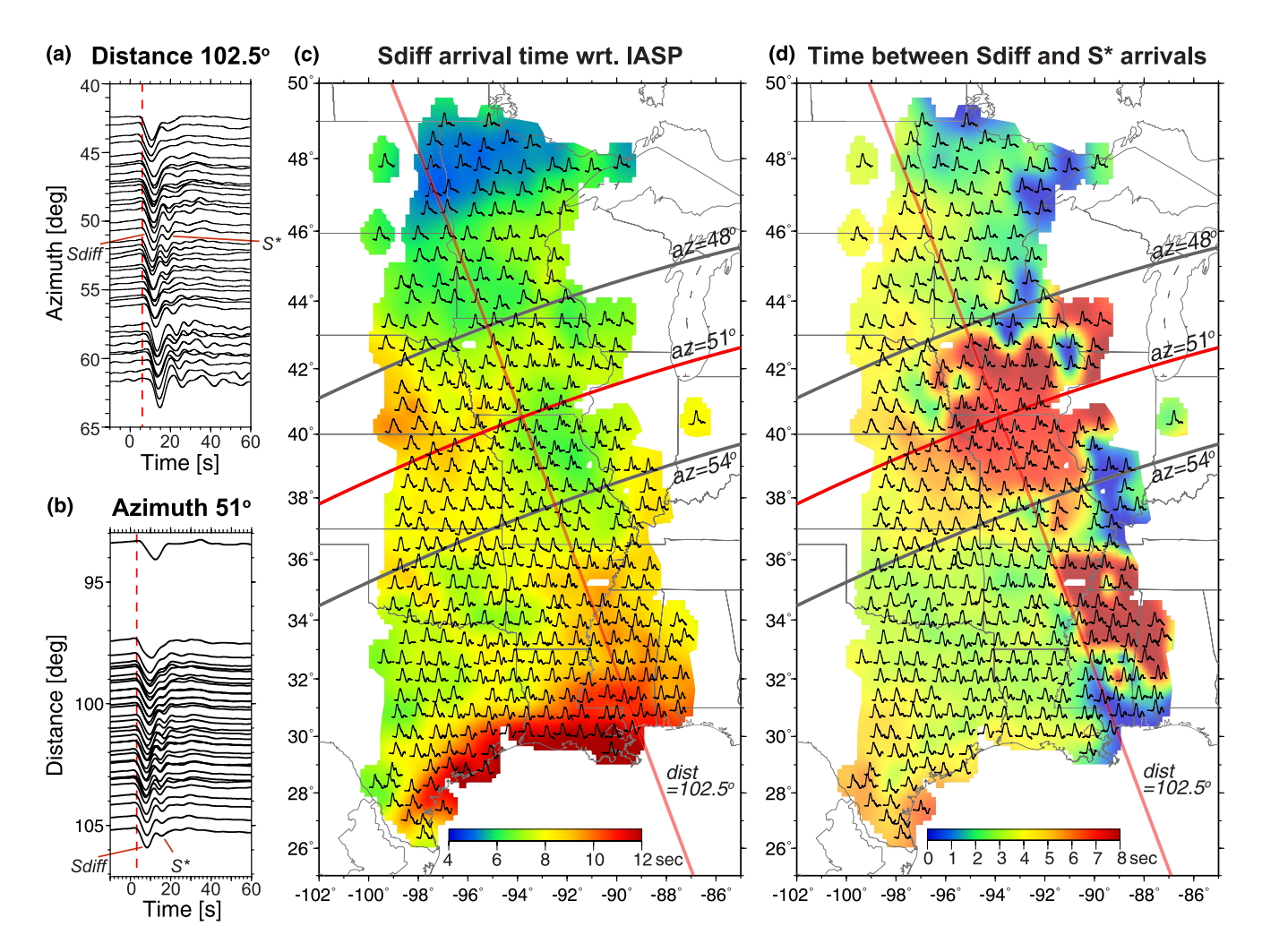


Figure 2. Multipathing behavior of Sdiff phase observed in Event A. (a) Record section shows Sdiff waveforms, filtered at 5–80 s, at distance 102.5° across a range of azimuths. S* is observed at azimuths 48° - 54° and after 60°. (b) Record section shows Sdiff waveforms at azimuth of 51°. S* most pronounced at distances greater than 100°. The waveforms are aligned at the expected Sdiff arrival time based on IASP travel time. (c) Color map shows the arrival time of Sdiff from Event A at the USArray stations with respect to the IASP model overlaid with their respective tangential displacement waveforms (d) Color map shows the measured time lapse between Sdiff and S* using the multipath detector (Sun et al., 2009). The phenomenon of S* is most prominent between azimuth 48° and 54°.

pulse with a time lag and a constant amplitude factor. The time delay of Sdiff relative to the reference IASP model (Figure 2c) and the time difference between Sdiff and S* (Figure 2d) are then measured by grid search. The strong multipathing occurs along a narrow range of azimuths between 48° and 54° (Figure 2d). From synthetic multipath detector tests (Sun et al., 2009), we can exclude out-of-plane structure as such structure generates strong multipathing only along its edges, which is not observed. For Event A, in-plane multipathing dominates the waveform distortion in the middle portion of the strong multipathing zone, that is, near the azimuth of 51° , which suggests the change in velocity gradient is along the ray path. There is also no significant change in Sdiff arrival time with respect to the IASP model across the boundary at azimuth 48° (Figure 2c), which further suggests the multipathing is caused by a localized anomaly. We tested a range of bandpass filters from 80 s up to 15, 10, 8, 5, and 2 s (Figure S2 in Supporting Information S1) and showed that the multipathing effect is only observable at shorter period (less than 8 s), which means tomographic models that use long period waves (>15 s) have difficulty to image these fine-scale lateral variations.

This S^* phase has been pointed out previously by To et al. (2011) as Phase "B" and is thought to be generated by a 2D structure along the great-circle plane, but the phase is not modeled in their study. The S^* multipathing is distinct from other observations of Sdiff postcursors, for example, those in Cottaar and Romanowicz (2012) where the postcursors arrive at a much later time (>20 s) with a move-out as a function of azimuth. These

LAI ET AL. 4 of 19



postcursors are formed out-of-plane due to a lens-like diffraction by a mega-sized ULVZ structure. In our case, the characteristics of the multipathing including the short arrival time of S^* (Figure 2b), the lack of the azimuthal move-out (Figure 2a), and its observability only at short period (Figure S2 in Supporting Information S1) suggest the S^* waveforms are unlikely to be a product of diffraction but distorted by a slow localized anomaly along the great-circle plane, in line with To et al. (2011).

2.2. S and ScS Observations

Velocity anomalies in the deep mantle can be detected using differential ScS-S travel time as S and ScS share similar ray paths particularly at the source and receiver ends, leaving only the deep mantle where the paths differ (Figure 3a). Both Events B and C record anomalous ScS and S behavior at distances between 75° and 90° along the same ray path where S* is observed. The variation along azimuth becomes evident when the arrival times of S and ScS at each individual station are shown with respect to IASP in map view (Figure 3). We observed strong anomalous delays for both S and ScS arrival times at stations in southwest USA along the azimuth of about 50° . For S, the strongest delay is centered at a distance of $\sim 84^{\circ}$.

We further measured the differential ScS-S travel time by taking the time difference between the ScS and S peaks. The strongest delay for ScS is centered at a closer distance and not co-located with S, resulting in a steep change in the differential ScS-S travel time, where the differential travel time is larger than expected from 1-D model at closer distance and smaller at larger distance. Record sections using two different stacking methods also show a consistent rapid variation in differential travel time along this azimuth (Figures S3 and S4 in Supporting Information S1). This differential travel time pattern is consistent for both events B and C, although there are slight differences in the individual S and ScS patterns due to small sampling difference in the lowermost mantle. In terms of waveform shape, we observed complicated ScS in regions with anomalous travel time behavior with mixed arrival times (Figure S5 in Supporting Information S1) and dampened amplitude (Figure S6 in Supporting Information S1).

The anomalous delay in S and ScS arrival times at two separate locations along azimuth $\sim 50^{\circ}$ suggests there may be multiple, distinct structures in the lowermost mantle impacting S and ScS independently. In contrast, we observed a localized delay of S and ScS at Yellowstone region (N 44°, W 111°). The delays are co-located, hence the differential travel time is not affected. The co-located delay is a result of a slow anomaly sampled by both S and ScS phases, most likely located in the upper mantle beneath Yellowstone. The presence of multiple structures could explain the rapid change in differential ScS-S travel time behavior: a slow structure at a closer distance to delay the travel time of ScS (i.e., increasing the differential travel time) and fast structure at later distance to speed up the travel time of ScS (i.e., reducing the differential travel time). There could also be shallower structures that affect S and not ScS, which explains the delay of S independent of ScS.

2.3. Summary of Observations

The observations of (a) multipathing of Sdiff, (b) rapid variation of differential ScS-S travel time and (c) the delay of S independent of ScS, all occurring along the same azimuth, are strong indicators of complex interaction among several distinct structural anomalies in the lowermost mantle at the northeastern edge of the Pacific LLSVP, about 12° southeast of Hawai'i (N 10°, W145°). There are several candidates in the lowermost mantle that could contribute to multipathing and travel time variation, including slow ULVZ-like structures proposed by previous seismic studies, fast structures such as slab debris, and the velocity variation across the edge of LLSVP. In the following section, we will use 2-D waveform modeling to explore these candidates and present possible models to explain the observations.

3. Waveform Modeling

Most global tomography models consistently show LLSVPs in the lowermost mantle, but the fine-scale structures, especially along the edges, vary between models and remain hard to be constrained. In this study, we built our models on the GyPSuM Model (Simmons et al., 2010), which is the preferred model in He and Wen (2012), as the GyPSuM model best accounts for the travel time of S and ScS, and their multiples. The GyPSuM model also incorporates the complex S velocity upper mantle structure beneath the western US by including the transition

LAI ET AL. 5 of 19



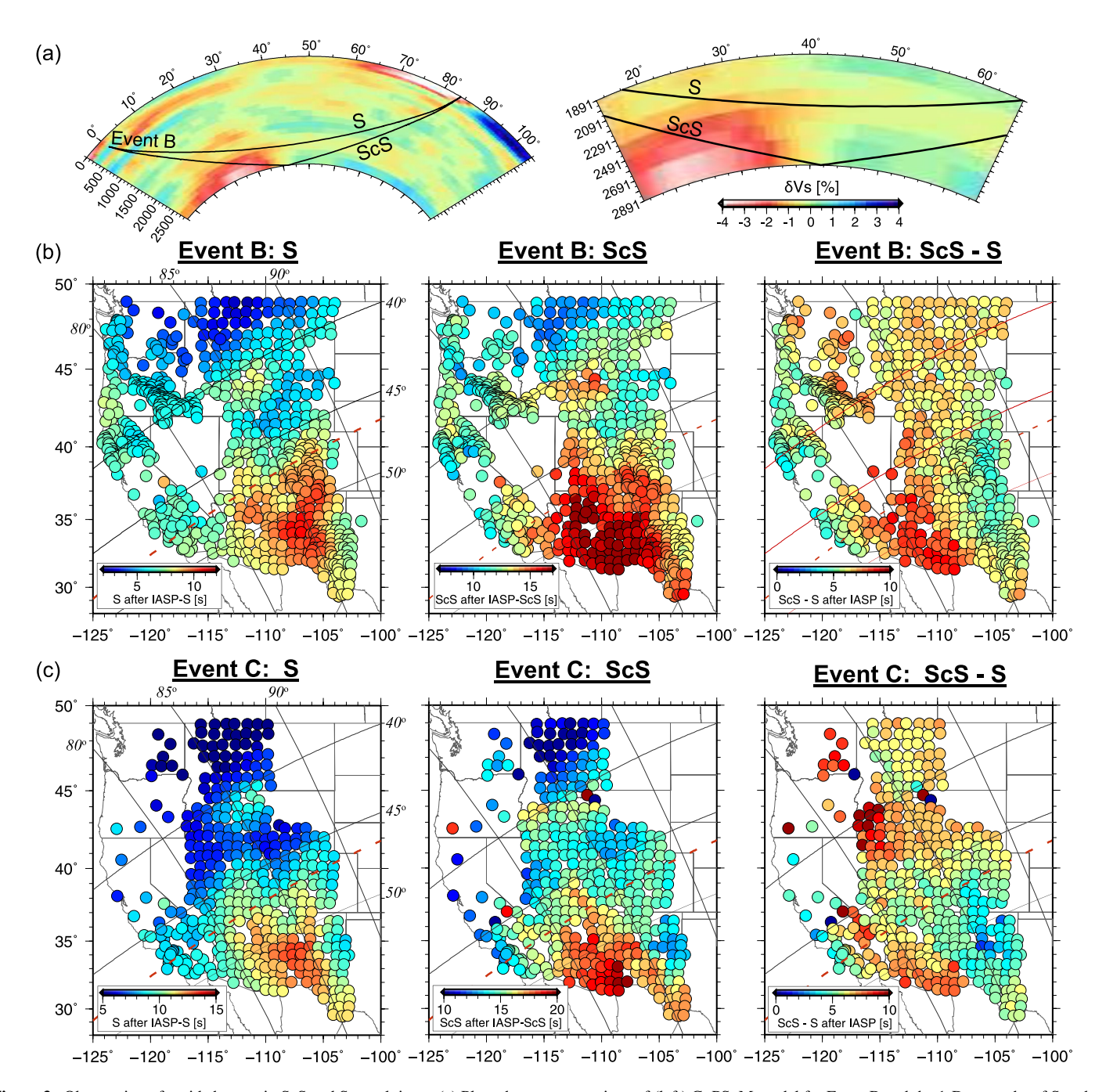


Figure 3. Observation of rapid changes in ScS and S travel times. (a) Plots show cross-sections of (left) GyPSuM model for Event B and the 1-D ray paths of S and ScS recorded at distance of 84° and (right) a close-up of S and ScS turning at the lowermost mantle. (b) Maps show the arrival time of (left) S and (middle) ScS, and (right) differential ScS-S time at each station for Event B, with respect to the expected arrival time based on 1-D IASP velocity model. Dashed red line corresponds to azimuth 48° for Event A, marking the edge where Sdiff phase begins to show multipathing. (b) Similar map for Event C, showing consistent pattern of rapid variations in differential ScS-S time. Record sections along constant azimuths can be found in Figure S3 in Supporting Information S1 (Event B) and Figure S4 in Supporting Information S1 (Event C).

from tectonic (TNA) to shield (SNA) model (Grand & Helmberger, 1984). The waveform synthetics are generated using a 2-D finite difference (FD) method (Li, Helmberger, et al., 2014) that can efficiently model global seismograms and core phases up to 3 Hz (Li, Sun, & Helmberger, 2014). As shown in observation, the anomalies are along the ray path and therefore can be modeled in 2-D. We set the FD grid size to 1.5 km and time step to 0.025 s to have waveforms accurate up to a period of 2 s. The source mechanisms are obtained from the USGS W-phase earthquake catalog, and the synthetics are convolved with triangle functions to account for the source

LAI ET AL. 6 of 19



time functions. The plotted tangential displacement waveforms are filtered at a period of 5–80 s. Considering the complex lateral variation of fine-scale structures along the edge of LLSVP, our 2-D modeling process will use as few parameters as possible to demonstrate the necessity of fine-scale structural anomalies at the north-eastern edge of the Pacific LLSVP and identify features of the structural anomalies that can be constrained by the observations.

3.1. Modeling of S*

The observed multipathing of Sdiff is not easily explained without strong localized anomalies, as suggested by To et al. (2011). Based on the simulation result of Event A, neither GyPSuM model (Figure 4) nor GyPSuM with inflated velocity perturbations (Figure S7 in Supporting Information S1) can reproduce the multipathing. From the simulation snapshot (Figure 4a), a ULVZ-like slow anomaly at the CMB not only slows down S and ScS wavefronts but also generates an additional pulse S*, which can be thought of as a secondary ScS. A fast anomaly, modeled at $\delta Vs = +5$ and $\pm 10\%$, produces no to very weak arrival before the main Sdiff phase and cannot replicate the observed multipathing.

Previous forward modeling results showed a variety of velocity reductions and geometries of ULVZs in this region, ranging from a ULVZ with a gradient velocity structure (δ Vs from top to bottom -3 to -5%; 60 km thick; He & Wen, 2012) to a ULVZ with a uniform velocity reduction (δ Vs = -30%; 10–20 km thick; Zhao et al., 2017). In this study, we investigated ULVZ parameters that could affect the waveform shape of the multipathing, that is, the location of the ULVZ with respect to the edge of the LLSVP, its velocity reduction, its width, and its thickness. Examining the width, we found that a minimal ULVZ width of 2 degree is needed to produce weak multipathing, and ULVZs with width up to 7 degrees can produce multipathing with the similar amplitude ratio between S and S*, that is, strong S paired with weak S* (Figure 5). Greater than 10 degrees, the waveform shape becomes distorted and contains multiple late-arriving pulses due to reverberation within the slow ULVZ. The width of the ULVZ which best matches the observed waveforms is 5 degrees.

The S* is sensitive to the location of the ULVZ. Fixing ULVZ width to 5 degrees, we tested the location of the ULVZ with respect to the edge of the LLSVP and found that the ULVZ can be uniquely constrained to the inner edge of the LLSVP, with the best fitting starting location at 35 degrees (Figure 6). A ULVZ toward the outer edge

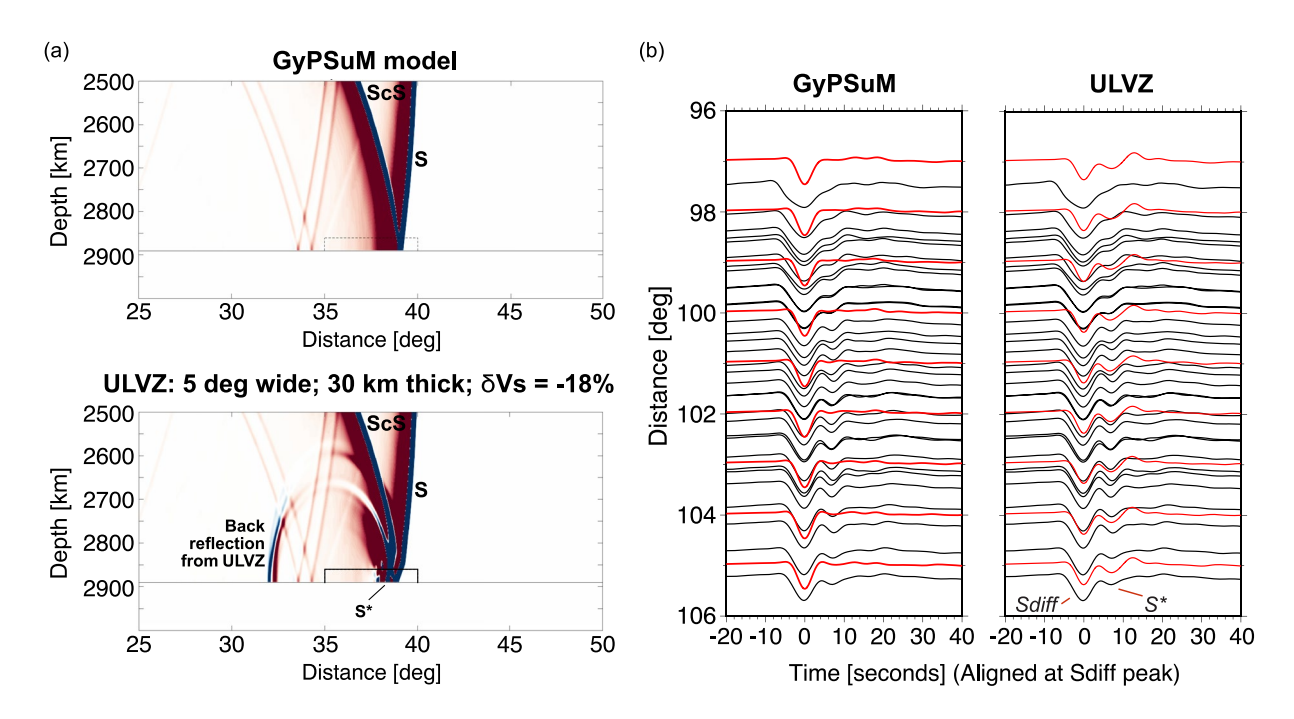


Figure 4. Multipathing due to localized ultra-low velocity zone (ULVZ) anomaly. (a) Simulation snapshots of Event A at the same time step from (top) the GyPSuM model and (bottom) a ULVZ-like structure (5 degrees wide; 30 km thick; $\delta Vs = -18\%$) embedded within the GyPSuM model. (b) Record sections comparing the waveforms observed during Event A (black) and synthetics from the two simulations (red). The waveforms are aligned at the main Sdiff peaks.

LAI ET AL. 7 of 19



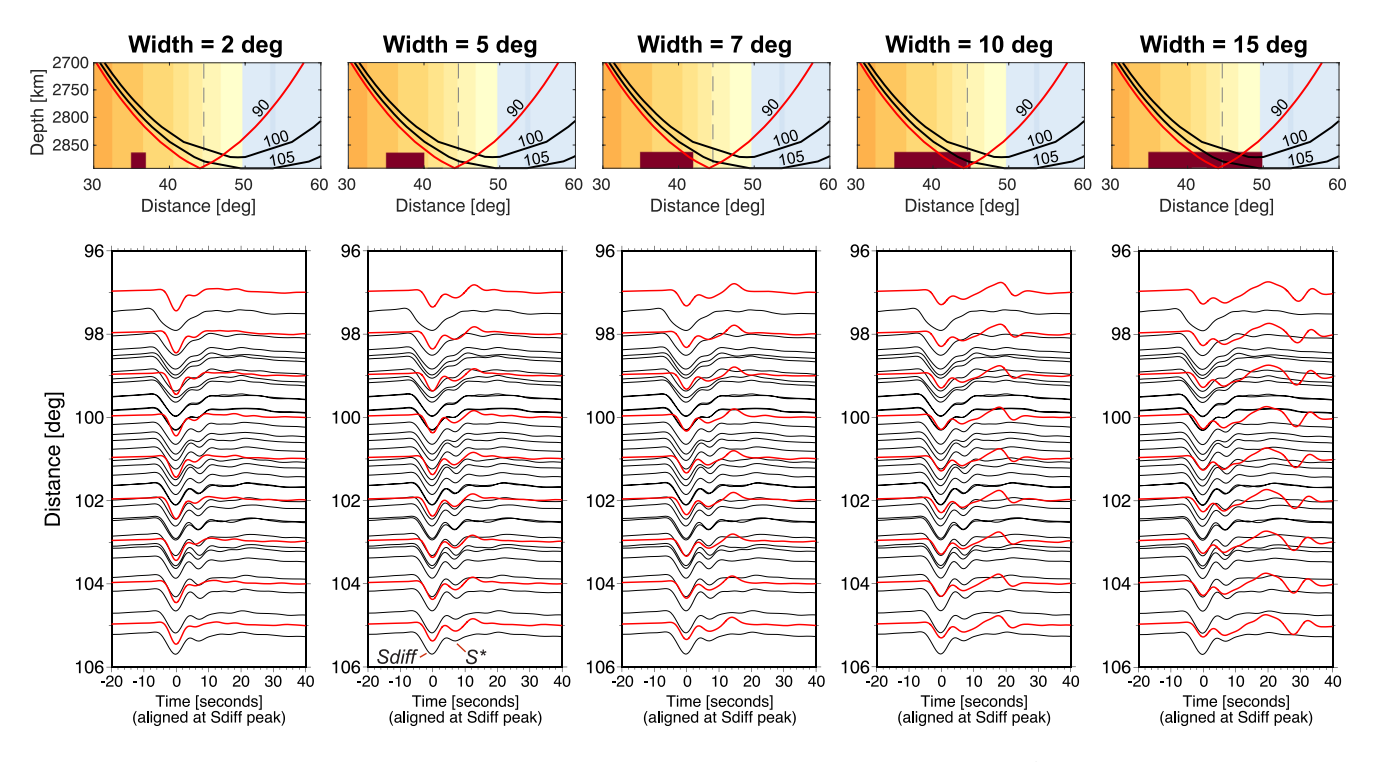


Figure 5. Ultra-low velocity zone (ULVZ) with different widths. (Top) Cross-sections of ULVZs (30 km thick; $\delta Vs = -18\%$) with five different widths (2, 5, 7, 10, and 15 degrees) embedded within the GyPSuM model at a fixed starting location of 35 degrees. The dashed gray line represents the contour for $\delta Vp = -0.4\%$, a proxy for the edge of the Pacific LLSVP. The 1-D ray paths for S (black), ScS (red), and Sdiff (black) are plotted using the 1-D IASP model at infinite frequency to serve as a rough guide. The presence of strong anomalies can bend ray paths and distort waveforms not directly on the ray path. (Bottom) Record sections comparing waveforms from Event A (black) and synthetics from the five ULVZ models (red).

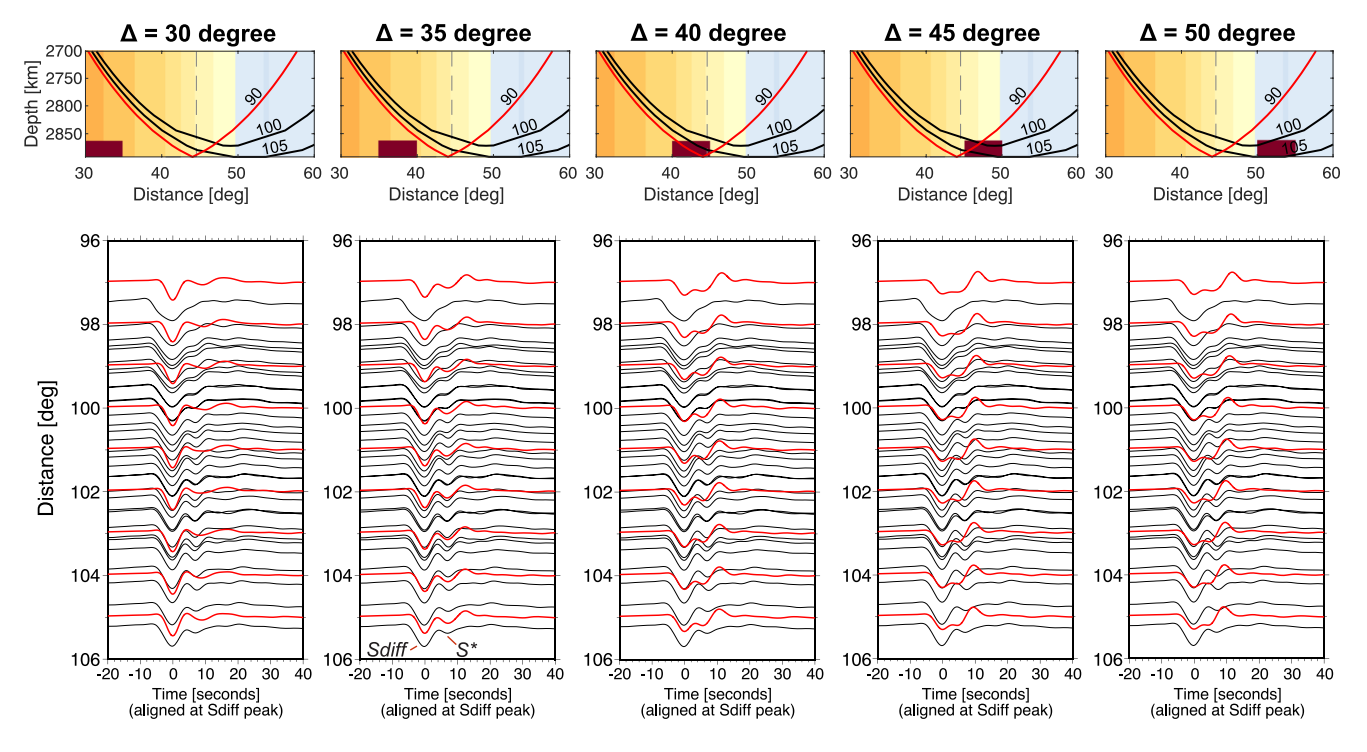


Figure 6. Ultra-low velocity zone (ULVZ) of fixed width at different distances. (a) Cross-sections of ULVZs (5 degrees wide; 30 km thick; δ Vs = -18%) embedded within the GyPSuM model at five starting distances: 30° , 35° , 40° , 45° , and 50° . (b) Record sections comparing waveforms from Event A (black) and synthetics from the five ULVZ models (red).

LAI ET AL. 8 of 19



Table 1The Goodness of Fit Between Data From Event A and Synthetics for Different Combinations of Velocity Reduction and ULVZ Thickness at a Distance of 102°

		1	ULVZ thickness (starting distance = 35°; width = 5°)					
Goodness of fit at distance = 102°		10 km	15 km	20 km	30 km	40 km	60 km	
δVs	-5%	-	-	0.0375	-	0.0359	0.0347	
	-10%	-	-	0.0340	0.0245	0.0181	0.0106	
	-12%	-	-	0.0260	0.0156	0.0108	0.0067*	
	-15%	-	-	0.0141	0.0082	0.0072*	0.0102	
	-18%	0.0286	0.0135	0.0086	0.0079*	0.0109	0.0211	
	-20%	0.0221	0.0103	0.0079*	0.0099	0.0150	0.0297	
	-23%	0.0154	0.0085	0.0087	0.0142	-	-	
	-25%	0.0128	0.0081*	0.0102	0.0179	0.0235	0.0451	
	-28%	0.0107	0.0090	-	-	-	-	
	-30%	0.0096	0.0120	0.0154	-	0.0183	0.0382	
	-33%	0.0081*	0.0156	-	-	-	-	
	-35%	0.0085	0.0140	-	-	-	-	

Note. The ULVZ width is fixed at 5° and its starting distance is fixed at 35°. The best-fitting combination for each thickness is marked with asterisks.

of the LLSVP generates stronger S* relative to Sdiff which is inconsistent with the observed waveforms. The edge of the LLSVP is defined by the -0.4% P-wave iso-velocity contour of GyPSuM, which best fits the boundary measured using Pdiff wave (Frost & Rost, 2014) and S-waves travel-times residuals (He & Wen, 2012).

There is an inherent trade-off between the ULVZ thickness and its velocity reduction (Thorne & Garnero, 2004), which particularly affects modeling efforts based on travel time. Fixing the width and starting location of the ULVZ, we investigated ULVZs of different thicknesses and velocity reductions. To determine the fit between the observed multipathing and synthetics, we measure the Goodness of Fit (GOF) between data from Event A and synthetics for different ULVZ models at distance 102° which is representative of the multipathing behavior. Lower GOF value means better match in pulse width and amplitude. The results, summarized in Table 1, show that the trade-off exists for the multipathing. There are a few combinations that can replicate the observed multipathing with a similar S* pulse width, comparable amplitude ratio between Sdiff and S*, and no additional strong late arrivals (Figure 7). Generally, the thicker the ULVZ, the weaker its velocity reduction is. However, the stronger velocity reduction means stronger velocity contrast with the surrounding mantle and tends to generate additional weak ripple-like arrivals after S*, and hence is less preferable. Our preferred ULVZ combination is 30 km thick with a velocity reduction of 18%, which can be reconciled with mineralogical modeling in Section 4.1. We note that a coarsely-structured gradient model also fits the waveforms well, at the expense of introducing more adjustable parameters and significantly larger uncertainties in the interpretation of such a structure. Our choice to assume a uniform ULVZ structure has the benefit of fewer adjustable parameters and lets us explore, through mineralogical modeling, well-defined tradeoffs and uncertainties in our interpretations.

We further investigated the potential trade-off between the ULVZ width and velocity reduction, fixing the thickness at 30 km and the starting distance at 35° (Table S2 in Supporting Information S1). We found that a very weak trade-off exists where a ULVZ of smaller width requires a stronger velocity reduction and vice versa. A 2-degree wide ULVZ model can generate multipathing with stronger velocity reduction at 30% but overall, the 5-degree wide ULVZ model produces the best fit. Ultra-low velocity zone models which are wider than 10° generally generate synthetics with strong reverberations that do not fit the observation, regardless the velocity reductions. No multipathing is observed for velocity reduction at -5%.

Overall, the modeling results suggest that the Sdiff multipathing can be best explained by a ULVZ structure located at the inner edge of the Pacific LLSVP, with a width between 2° and 7° (120–430 km at the CMB). The location and width of ULVZ are well-constrained and consistent for all the best-fitting thickness-velocity

LAI ET AL. 9 of 19



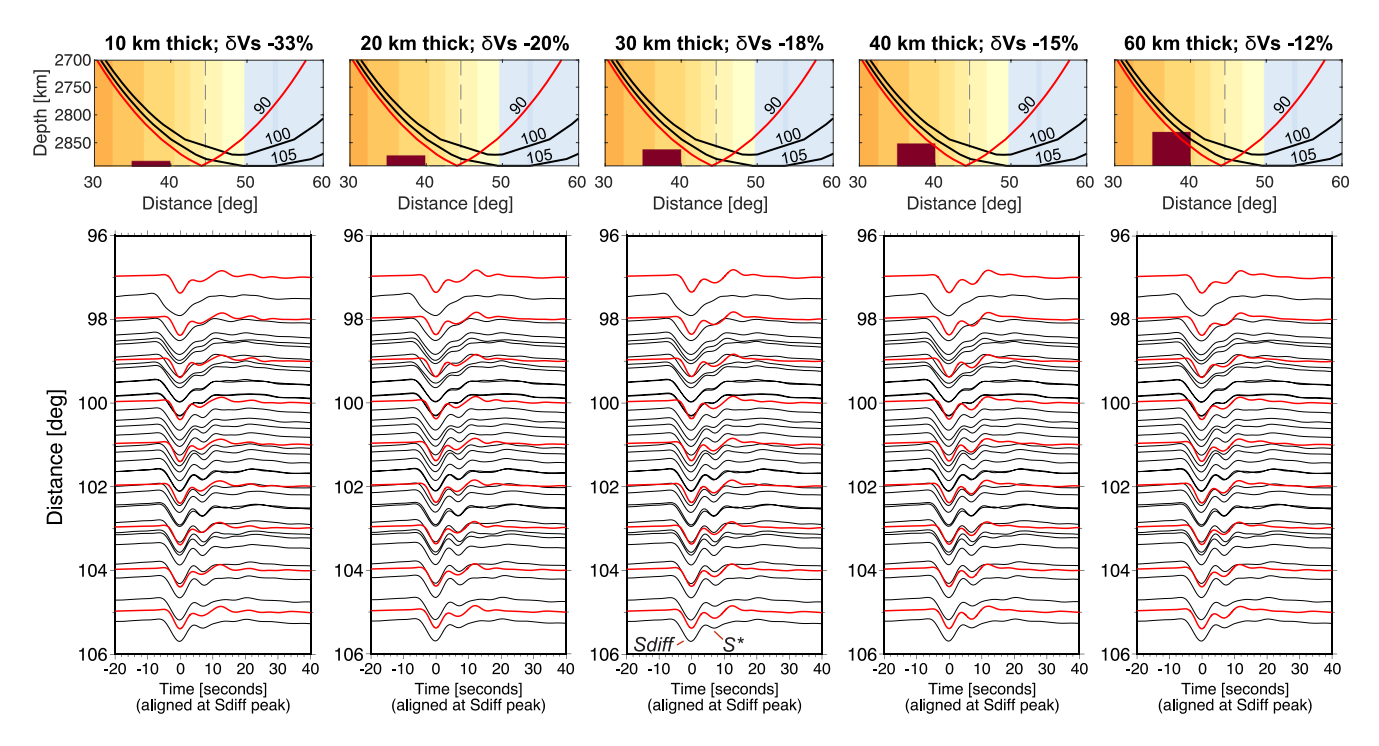


Figure 7. Ultra-low velocity zone (ULVZ) with different combinations of thicknesses and velocity reductions. (a) Cross-sections of ULVZs with five different combinations of thickness and the corresponding best-fitting velocity reductions. The starting location and width are fixed at 35 and 5° respectively. (b) Record sections comparing waveforms from Event A (black) and synthetics from the five ULVZ models (red).

reduction combinations (Table S2 in Supporting Information S1). For the subsequent sections, the ULVZ is modeled to be 5° wide, 30 km thick with a shear wave velocity reduction of 18% at a starting location of 35 degree.

3.2. Modeling of Differential ScS and S Travel Time

The rapid variation in differential ScS-S travel time, where the time is slower than expected at closer distances and faster at larger distances, could not be simply explained by the velocity contrast across the edge of the LLSVP. Focusing on Event B, the synthetic ScS simulated using the GyPSuM model arrives about 4 s earlier than observation (Figure 8a). Considering that the velocity perturbation in the tomography model may be underestimated, we tested a model where the velocity perturbation for the bottom 800 km is inflated by a factor of 2 and found that it can delay the ScS arrival and better match the observed differential ScS-S travel time (Figure S8 in Supporting Information S1). However, the differential time behavior is localized along a short azimuth band and cannot be explained by a blanket inflation of velocity perturbation in the lowermost mantle. The inflation also cannot preserve ScS at large distances or explain the multipathing of S* (Figure S7 in Supporting Information S1).

On the other hand, the same ULVZ-like structure, which explains the multipathing of S*, can preserve ScS across large distances. The ULVZ also fits the differential ScS-S travel time for distance less than 80° but not that for distances larger than 84° (Figure 8b). To reduce the differential ScS-S time at large distances, we opt for adding a fast structure (δ Vs = +2.5%) adjacent to the ULVZ as it minimally affects ScS at closer distances and speeds up ScS at larger distances by 2–3 s (Figure 8c). The shape of the fast structure is designed to maximize the ray paths of ScS at distance greater than 84° within the structure. The fast structure is thought to be one of the high velocity anomalies imaged by many seismic tomography models surrounding the Pacific LLSVP in the lowermost mantle (Sun et al., 2019).

The delay of S independent of ScS (Figure 3) implies a possible slow structure in the lowermost mantle above the CMB which is preferentially sampled by S and not ScS. Such delay may be explained by a plume rising from the edge of the LLSVP, whose generation is made conducive with both the ULVZ and slab at the edge of the LLSVP (see discussion in Section 4.2). The plume-like structure is modeled to have a velocity reduction of 5%

LAI ET AL. 10 of 19



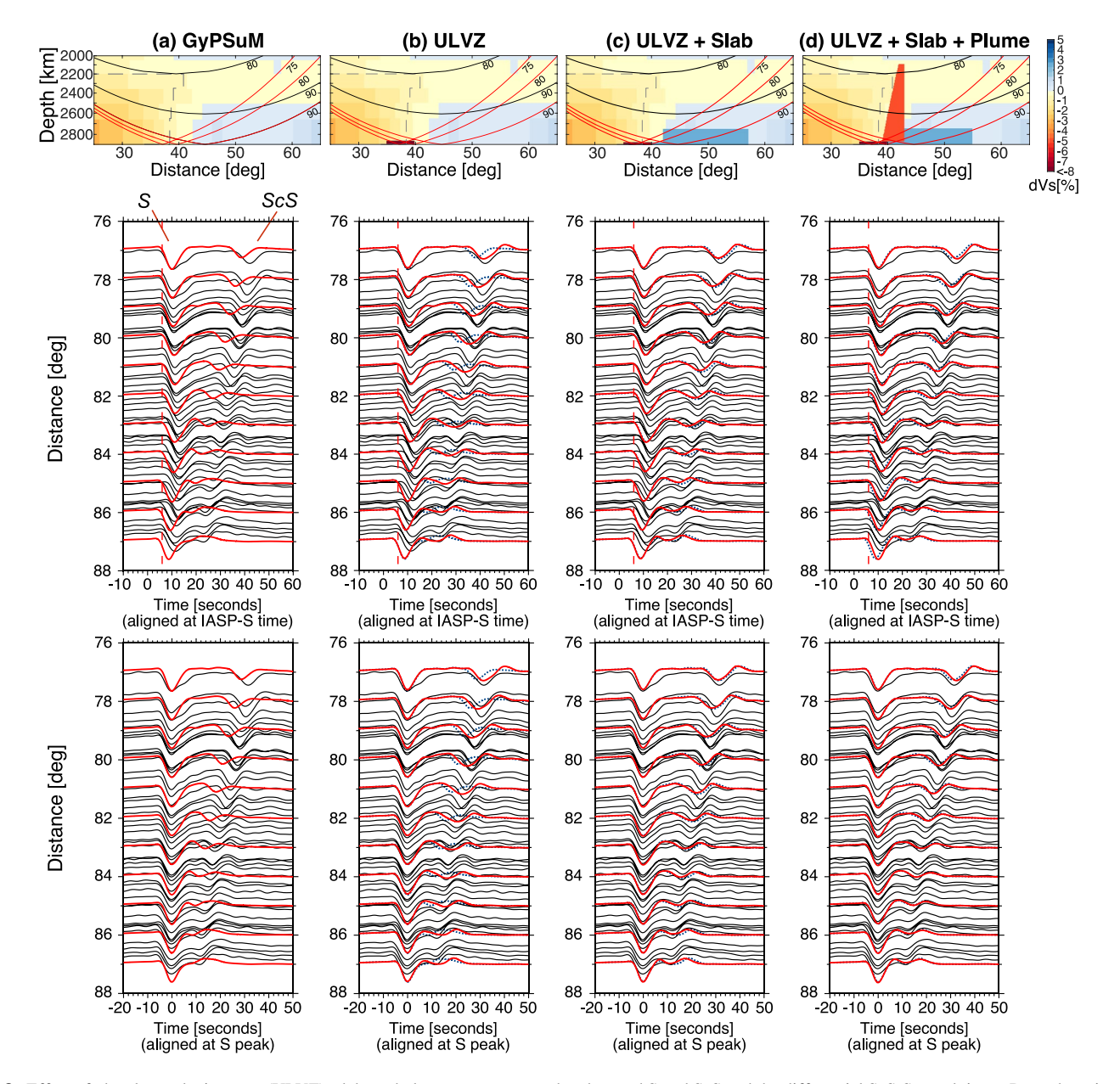


Figure 8. Effect of ultra-low velocity zone (ULVZ), slab, and plume structures on the observed S and ScS and the differential ScS-S travel times. Record sections show the stacked tangential data (black) from Event B and synthetics (red) aligned at (top) the expected IASP-S arrival time and (bottom) the peak of S pulse. The synthetics are generated from four models: (a) GyPSuM model, (b) GyPSuM model with a ULVZ-like structure (30 km thick; 5° wide; δ Vs = -18%) (c) GyPSuM model with the ULVZ plus a high velocity anomaly (150 km thick; 15° wide; δ Vs = +2.5%) (d) GyPSuM model with ULVZ, slab and an additional plume-like structure (800 km tall; 4° wide at the bottom; 1° wide at the top, δ Vs = -5%). Blue dashed lines in (b), (c), and (d) outline the waveforms from the prior models without the added structures for easier comparison.

and extend upward while narrowing in width to a height of \sim 800 km. The plume with narrowing width is chosen over that of uniform width as the narrowing width better fits the overall differential travel times by delaying the S arrival slightly by 2–3 s for distance between 83° and 86° (Figure 8d) and does not create additional multipathing in Event A (Figure S9 in Supporting Information S1).

Unlike the ULVZ parameters, which can be constrained with the S* multipathing, we do not attempt to overly refine the geometry and velocity of the high velocity anomaly and plume, given the modeling relies solely on the travel times of ScS and S. The true plume height cannot be estimated due to the lack of S observations at the shallower turning points (no stations in closer distances). The fit of the S delay can also be improved with a more complicated plume design supported by more observations. In summary, our modeling results show that

LAI ET AL.



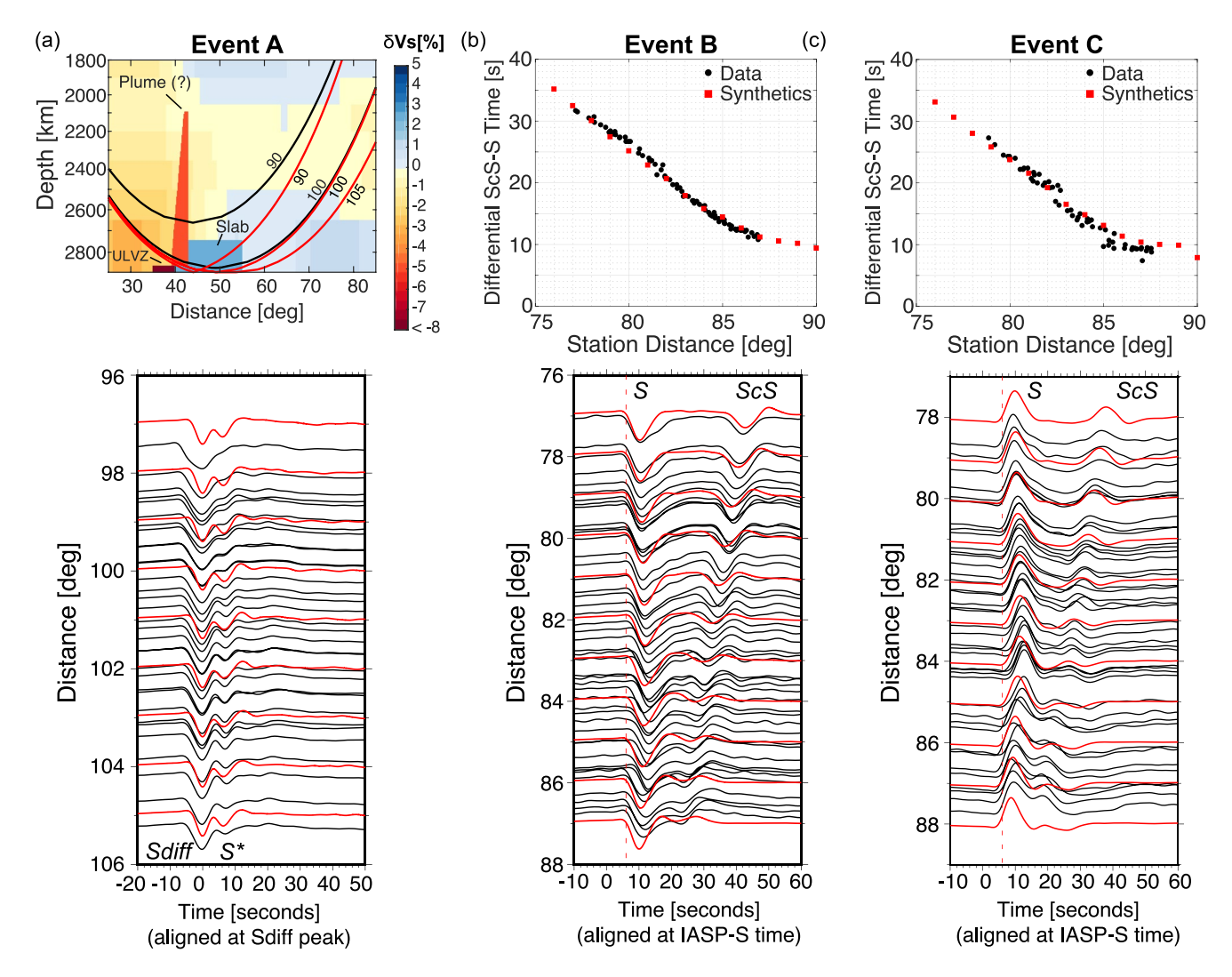


Figure 9. Modeling results for Event A, B and C. (a) Cross-section of the model: GyPSuM embedded with a ULVZ (30 km thick; 5° wide; $\delta Vs = -18\%$), a slab (150 km thick; 15° wide; $\delta Vs = +2.5\%$), and a possible plume structure (800 km tall; 4° wide at the bottom; 1° wide at the top, $\delta Vs = -5\%$). The 1-D approximate ray paths of ScS, S and Sdiff for Event A are plotted. The record section at the bottom shows the fit of S^* between the synthetics (red) and the data (black) for Event A. (b + c) Top graph shows the comparison of differential ScS-S time at azimuth $49-51^{\circ}$ measured from synthetics (red) and data (black) for (b) Event B at azimuth $49-51^{\circ}$ and (c) Event C at azimuth $50-52^{\circ}$. Bottom plot shows the waveform comparison of S and ScS between synthetics (red) and data (black). The waveforms are aligned at the expected S arrival time based on the 1-D IASP reference model.

a combination of ULVZ, high velocity anomaly, and plume, where the ULVZ is located close to the edge of the LLSVP with the slab structure outside of the LLSVP, can fit multiple observations including S* multipathing, rapid variation of differential ScS-S travel time, and independent delay of S for Event A, B, and C (Figure 9).

4. Discussion

Fine-scale structural variation at the edges of LLSVP remains difficult to image at long periods. By modeling body waves at short periods in 2-D, we can image potential complex interaction between multiple structural anomalies, where a substantial ULVZ located near the inner edge of the Pacific LLSVP, adjacent to a high velocity anomaly outside the LLSVP. The location of our proposed ULVZ, observed using Sdiff multipathing, is near the thickest ULVZ clusters seen in Zhao et al. (2017) and Jenkins et al. (2021), mapped using ScS core reflected phase, and consistent with the southern patch in Sun et al. (2019), observed in the multipathing of ScS but not modeled. The northern patch previously modeled by Sun et al. (2019) is not clearly observed in our data set due to the ray paths being out of range. The 2-D modeling also allows us to confirm the presence of slab outside of

LAI ET AL. 12 of 19



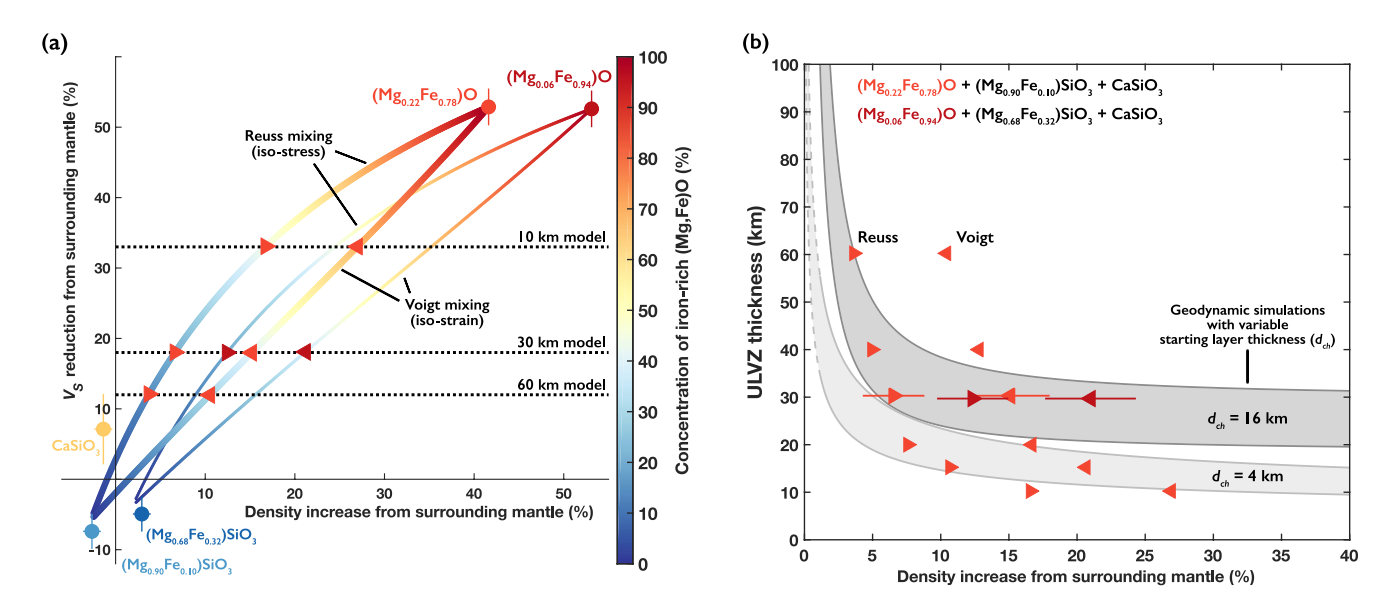


Figure 10. Mineralogical models of solid ultra-low velocity zones (ULVZs) containing iron-rich magnesiowüstite. (a) Forward models of velocity reductions relative to IASP at the CMB and density increases relative to PREM at the CMB for solid assemblages containing varying amounts of iron-rich (Mg,Fe)O magnesiowüstite mixed with (Mg,Fe)SiO₃ bridgmanite and CaSiO₃ at a constant ratio of 85:15. Thicker lines show (Mg_{0.22}Fe_{0.78})O (Mw78) + (Mg_{0.90}Fe_{0.10})SiO₃ + CaSiO₃ and thinner lines show (Mg_{0.06}Fe_{0.94})O (Mw94) + (Mg_{0.68}Fe_{0.32})SiO₃ + CaSiO₃. Assemblage properties are calculated for both Voigt (iso-strain) and Reuss (iso-stress) endmember mixing bounds. Dotted black lines indicate velocity reductions constrained by seismic modeling for different possible ULVZ thicknesses. Rightward (Reuss) and leftward (Voigt) triangles show resulting densities for assemblages that reproduce velocity reductions in each seismic model for Mw78 (light red) and Mw94 (dark red) bearing assemblages. Full phase elasticity information is given in Table S3 in Supporting Information S1. (b) Densities for assemblages that reproduce seismically modeled velocity reductions at each ULVZ height for Reuss (right triangle) and Voigt (left triangle) mixing and for Mw78 (light red) and Mw94 (dark red) bearing assemblages. Shaded regions indicate equilibrium thickness of solid ULVZs modeled by geodynamic simulations (Figure S12 in Supporting Information S1) as a function of ULVZ density, given a starting chemically distinct layer of thickness 4 km (light gray) and 16 km (dark gray).

the LLSVP, which has been hypothesized in Sun et al. (2019) and Jenkins et al. (2021) but was not modeled, and the role of slab in modulating the differential ScS-S travel times. The presence of the thin plume is hypothesized based on the observation of S travel time delay independent of ScS but is not well-resolved in our modeling. In the following sections, we will explore these proposed structures in three contexts: (a) the mineralogy of the ULVZ; (b) geodynamical implications of ULVZ-slab configuration near the edge of LLSVP; and (c) a potential way to improve plume imaging and its current limitation.

4.1. Mineralogy of ULVZ

The existence of the ULVZ structure could arise through several scenarios such as (a) the partial melting of ambient mantle or subducted slab materials (Liu et al., 2016; Pradhan et al., 2015; Thorne et al., 2019), and/or (2) a solid-state assemblage containing iron-enriched (Mg,Fe)O magnesiowüstite (Bower et al., 2011; Finkelstein et al., 2018; Wicks et al., 2017) that may be produced by chemical interaction with the core or magma ocean solidification (Labrosse et al., 2007). Recent work has demonstrated that the modeled seismic properties of various ULVZs are compatible with a solid magnesiowüstite-bearing assemblage (Dobrosavljevic et al., 2019; Jackson & Thomas, 2021). Here, we tested the solid magnesiowüstite hypothesis for the ULVZ detected in this study with the following steps: (a) construct forward models of magnesiowüstite-bearing assemblages to calculate bulk densities of assemblages that can reproduce the observed velocity reductions, given tradeoffs in thickness and velocity reduction in the seismic models (Figure 7); (b) compare resulting assemblage densities for each thickness-velocity reduction combination against geodynamic simulations of thickness dependence on density for solid ULVZs; and (c) invert for best-fit mineralogy for the preferred seismic model to determine the error correlations on compositions and bulk properties.

We first calculated forward models of the proposed mineralogies for two different magnesiowüstite compositions - $(Mg_{0.06}Fe_{0.94})O$ (hereafter Mw94) and $(Mg_{0.22}Fe_{0.78})O$ (hereafter Mw78)–shown in Figure 10a, using elastic properties calculated at CMB conditions for iron-rich (Mg,Fe)O magnesiowüstite with coexisting (Mg,Fe)SiO₃ bridgmanite and CaSiO₃ calcium silicate perovskite (see Table S3 and Figure S10 in Supporting Information S1;

LAI ET AL. 13 of 19



Dobrosavljevic et al., 2019). We varied the concentration of magnesiowüstite mixed with a constant 15:85 ratio of $CaSiO_3$ to bridgmanite. To account for uncertainty in stress distribution among the constituent phases, we calculate models using two endmember phase mixing cases - Voigt averaging (uniform strain distribution) and Reuss averaging (uniform stress distribution) (Watt et al., 1976). Because the elastic moduli of magnesiowüstite are much smaller than those of the other two constituent phases, the two mixing bounds exhibit large differences in bulk assemblage properties for a given magnesiowüstite concentration or a given bulk velocity reduction (Figure 10a, Figure S11 in Supporting Information S1).

As shown in Figure 10, we used the forward models to calculate bulk densities of Mw78-bearing assemblages that reproduce the best-fitting velocity reduction constrained for each thickness-velocity reduction combination in the seismic modeling (Figure 7), for both the Voigt and Reuss bounds, as well as for Mw94 in the case of the 30 km model. By doing so, we investigate how tradeoffs in the seismic modeling of ULVZ properties can lead to a range of possible mineralogies and ULVZ densities. Resulting density uncertainties (Figure 10b) are propagated from uncertainties in the seismic velocity reduction (estimated at 3%) and uncertainties in the mineral densities (<1%). The dominant source of uncertainty in these mineralogical models comes from whether the assemblage is under conditions that are closer to the Voigt or Reuss bound. Given the very low elastic moduli of magnesiowüstite and its very low viscosity (Reali et al., 2019), these assemblages may be closer to the Reuss bound, which exactly describes the effective moduli of solid grains suspended in a fluid with zero shear modulus (Mavko et al., 2010). However, due to a lack of experimental data on the elastic and rheological properties of such ironrich assemblages at lower mantle conditions, we consider both the Voigt and Reuss bounds in our analysis.

Next, we investigated whether the calculated mineral assemblage densities for each possible ULVZ thickness are compatible with geodynamic simulations that constrain thickness dependence on density for solid-state ULVZs (Bower et al., 2011). In these geodynamic simulations, a steady-state ULVZ morphology is derived from an initial chemically distinct dense layer between 4 and 16 km thickness (see Figure S12 in Supporting Information S1). Given the potential dynamic complexity in this study region, we note that the result from modeling the ULVZ as steady state in the absence of dynamic upwelling or downwelling is an approximation. The ULVZ thickness (Figure 10b) depends on the density of the chemically distinct ULVZ material, modeled as an assemblage containing low magnesiowüstite (Reali et al., 2019). This analysis shows that the taller ULVZ seismic models are compatible only in the case of Reuss mixing. Ultra-low velocity zone models thinner than 20 km are also compatible with geodynamic simulations in the case of a thinner starting chemical layer. However, as discussed in Section 3.1, these models are less preferable as they generate additional weak ripple-like arrivals after the S* pulse that are not observed. The 30 km model is preferred as it can be explained by a solid magnesiowüstite-bearing ULVZ for both cases of Voigt and Reuss mixing and for both Mw78 and Mw94 compositions.

Finally, using a best-fit minimization approach, we inverted for assemblage compositions most compatible with the preferred seismic model (30 km thickness, -18% δVs) and examined the error correlations for the modeled mineralogy (see Dobrosavljevic et al. (2019) for details of the inversion method). The inversions incorporate uncertainties from mineral physics on phase elasticity (Table S3 in Supporting Information S1) as well as uncertainties on seismic velocity (estimated at 3% from Table S2 in Supporting Information S1). As this study only constrains δVs values for the ULVZ, we estimate density and δVp values from the forward models for use in the inversion and assign a larger 5% uncertainty. Inversion results for Mw78 and Mw94-bearing assemblages are shown in Figure 11 and Table S4 in Supporting Information S1, with ellipses representing correlated uncertainties at the 1σ level for Voigt (dashed lines) and Reuss (solid lines) mixing. The concentration of magnesiowüstite is relatively tightly constrained (1%-2% uncertainty), while the concentration of bridgmanite shows more uncertainty and tradeoff with the concentration of CaSiO₃ (Figure 11a). Even for the most iron-rich assemblage (Mw94 Voigt) constrained in this analysis (Table S4 in Supporting Information S1), an initial 16 km chemical layer at the CMB would produce no more than a ~0.1 wt% increase in the total FeO content of the whole mantle, well within the uncertainty of the previously estimated bulk silicate earth value of 7.97 ± 0.54 wt% (Lyubetskaya & Korenaga, 2007), based on a statistical analysis. By considering the error correlations in the resulting seismic velocities of the assemblages (Figure 11b), we showed that such solid magnesiowüstite-bearing assemblages can produce a range of δVs : δVp ratios, from ~ 1.2 up to the ~ 3 ratio level commonly attributed to the presence of partial melt (Berryman, 2000).

In short, we constructed a mineralogical model for the observed ULVZ containing solid iron-rich (Mg, Fe) O magnesiowüstite. This model is consistent with three independent constraints: (a) the seismically modeled

LAI ET AL. 14 of 19



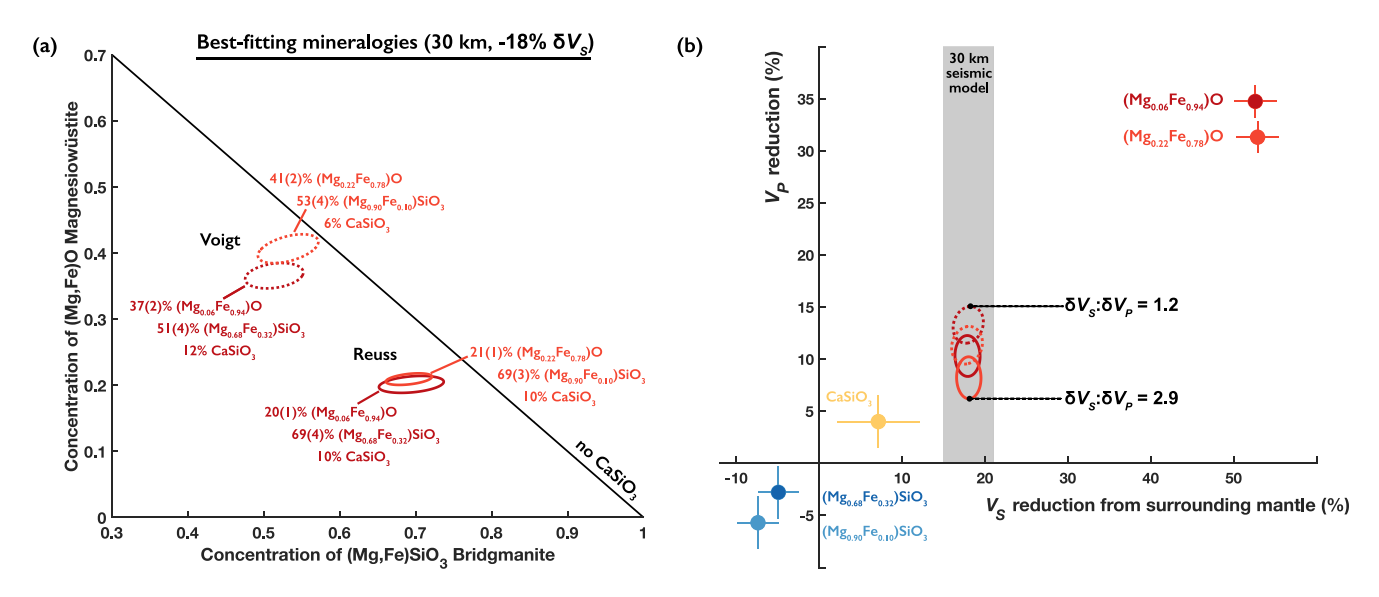


Figure 11. Best-fitting mineralogies for the preferred seismic ultra-low velocity zone (ULVZ) model. (a) Composition results from inversions for best-fitting mineralogical assemblages containing ($Mg_{0.2}Fe_{0.78}$)O (Mw78) (light red) and ($Mg_{0.06}Fe_{0.94}$)O (Mw94) (dark red) mixed with coexisting bridgmanite and CaSiO₃, calculated for both Voigt (dotted lines) and Reuss (solid lines) bounds for the preferred seismic ULVZ model (30 km thickness, -18% δVs). The diagonal black line represents cases where the concentration of CaSiO₃ is zero. For the region below the diagonal black line, the concentration of CaSiO₃ is 1 minus the sum of the concentrations of magnesiowüstite and Bridgmanite. Labels indicate relative concentrations of constituent phases with uncertainties. Ellipses indicate correlations in the concentration uncertainties at the 1σ level. Full results are given in Table S4 in Supporting Information S1. (b) Aggregate velocity reductions relative to IASP at the CMB for the best-fitting assemblages shown in (a). Gray shading indicates the velocity reduction of the preferred seismic model with 3% uncertainty estimated from Table S2 in Supporting Information S1. Correlated velocity reduction uncertainties for Voigt (dotted lines) and Reuss (solid lines) bounds for Mw78 (light red) and Mw94 (dark red) bearing assemblages span a range of δVp values and produce δVs: δVp ratios from ~1.2 up to the ~3 ratio level commonly attributed to the presence of partial melt.

δVs and thickness of the ULVZ, (b) phase elasticities and viscosities from mineral physics, and (c) ULVZ morphologies from geodynamic simulations. These results together provide strong quantitative support for a solid-state magnesiowüstite-bearing ULVZ interpretation and show that partial melt is not necessary to produce the observed ULVZ properties. A possible partial melt origin is not assessed nor ruled out in this analysis but may face challenges from recent geodynamic simulations (Dannberg et al., 2021) and a lack of *in-situ* experimental data on the sound velocities of partially molten assemblages. Though the rheology of the modeled solid iron-rich phase assemblage is uncertain, recent findings have suggested the development of an interconnected weak layer (IWL) of iron-poor (Mg, Fe)O ferropericlase coexisting with bridgmanite at lower mantle conditions (Chandler et al., 2021). In comparison, iron-rich (Mg, Fe)O exhibits even lower viscosities (Reali et al., 2019), which may further promote IWL formation, as well as much higher conductivities (Ohta et al., 2014). The possibility of highly conductive, interconnected magnesiowüstite in the ULVZ could lead to an increased bulk thermal conductivity of the structure and contribute to enhanced plume generation.

4.2. Geodynamical Implication

The edges of LLSVPs are particularly of interest due to a putative spatial correlation with large igneous provinces, hotspots, and kimberlites from plate reconstructions (e.g., Burke & Torsvik, 2004; Torsvik et al., 2010). Yu and Garnero (2018) have found that ULVZs are more commonly found in the edges of LLSVP and near hotspots, although the correlation is not statistically robust. In our study, the ULVZ is located near the inner edge of LLSVP, suggesting a strong thermochemical convection toward the edge of LLSVP where ultra-dense compositionally distinct material preferentially accumulates (Li et al., 2017). The high velocity anomaly could potentially be a remnant of subducted slab descended into the lowermost mantle, supported by many seismic tomography models where high velocity anomalies are observed surrounding the Pacific LLSVP in the lowermost mantle. The presence of fast and cold slab could indicate a strong lateral temperature gradient across the LLSVP edge, promoting upwelling and triggering a long-lasting plume rising along the edge of the LLSVP (Jellinek & Manga, 2004; Tan et al., 2011; Figure 12). These locations also tend to have strong thermal instabilities due to the lowermost

LAI ET AL. 15 of 19



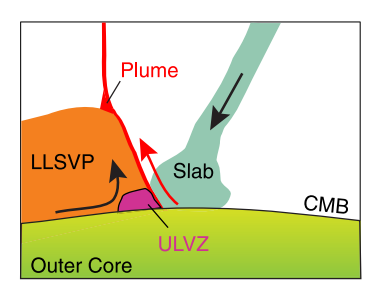


Figure 12. Schematic showing the preferred location of the ultra-low velocity zone (ULVZ) and slab near the edge of the Large Low Shear Velocity Province. A subducted slab, proposed by Sun et al. (2019) as well, encountering the edge of the Pacific LLSVP along the CMB and a ULVZ driven toward the interior of the LLSVP are conducive for mantle upwelling and plume generation.

mantle flow induced by subducted slab, hence strong plumes are preferentially located close to the edges of the LLSVP (Li & Zhong, 2017).

Our location of the ULVZ-slab interaction leading to a potential plume is consistent with the plume location in some flow models that successfully match the Hawaiian-Emperor hotspot track (Hassan et al., 2016). More recent plate reconstructions of the northern Pacific along with geodynamic models suggest that subduction from the late Miocene/early Tertiary occur at an intraplate subduction zone just north of the present location of Hawai'i (Hu et al., 2022), potentially a more favorable location of the seismically-inferred boundary of a plume and slab.

The combination of ULVZ and slab in proximity may also explain the complex shear wave anisotropy in this region. Relative travel times from shear wave splitting in S and Sdiff show strong variation in the strength of anisotropy with $V_{SH} > V_{SV}$ (Fouch et al., 2001) while the close arrivals of short period body wave phases (S, Scd, and ScS) gives an apparent anisotropy $V_{SV} > V_{SH}$ instead (Sun et al., 2019). The mixed measured anisotropy

may be due to a complex mantle flow pattern near the edge of the LLSVP (Reiss et al., 2019) and the presence of multiple anisotropic structures such as past subducted slab (Fouch et al., 2001) and a ULVZ composed of highly anisotropic magnesiowüstite (Finkelstein et al., 2018).

4.3. Imaging Potential Plume Structure

The direct imaging of a thin plume rooted in the lower mantle remains difficult due to multiple factors such as weak perturbation in travel time, ray paths sampling the deep mantle mostly normal to the plume direction, and wavefront healing effects (Maguire et al., 2016). In our study, a plume structure is proposed to explain the delay of S independent of ScS, but its characteristics is hard to constrain by solely modeling the short time delay (3–4 s) observed by ray paths normal to the plume. ScS and its multiples, on the other hand, sample the lower mantle and have been demonstrated useful to image plumes rooted in the lowermost mantle including that for the Yellowstone hotspot (Nelson & Grand, 2018). Multiple ScS with near vertical paths is particularly sensitive to the structural anomalies within a diameter of about 1,000 km across the whole mantle (Julian, 2005). The differential time between multiple ScS can differ greatly from a 1D model with the presence of structural anomalies as the travel time errors accumulate with each reflection. Therefore, these multiple ScS with vertical incident angles provide a unique way to test the hypothesis of broad vertical plume directly beneath hotspot proposed by several global tomographic studies (French & Romanowicz, 2015; Zhao, 2004).

Previous observations by Kanamori and Rivera (2015) showed that the multiple ScS travel time at Hawai'i is well-predicted by the PREM model, implying the shear wave speed beneath Hawai'i is similar to the average mantle, consistent with the findings from Best et al. (1974). Kanamori and Rivera (2015) also found that the Q structure, which is a proxy for attenuation due to thermal anomalies, is comparable to the average mantle. Meanwhile, the shear wave profile and Q structure are highly anomalous for other island stations, particularly beneath the Samoa hotspot (Montelli et al., 2006), which suggests the velocity structure directly beneath Hawai'i does not favor a broad thermal plume.

Using the 3D spectral-element method (Komatitsch & Tromp, 2002), we calculated the ScS multiple travel times from the 04 May 2018 M6.9 Hawai'i Island earthquake recorded on Hawaii for three representative global models, S40RTS (Ritsema et al., 2011), S362ANI (Moulik & Ekström, 2014), SEMUCB-WM1 (French & Romanowicz, 2014; Figures S13 and S14 in Supporting Information S1). For S40RTS and S362ANI, there is not a pronounced continuous slow structure beneath Hawai'i but some scattered slow anomalies, and we found that the synthetics of the multiple ScS from these two models are significantly delayed compared to the data (Figure S15 in Supporting Information S1). On the other hand, the travel time of the multiple ScS for SEMUCB-WM1 which images a broad vertical plume beneath Hawai'i fits the 1-D model. The apparent inconsistency may stem from the missing strong fast oceanic lithosphere and low velocity zone in the asthenosphere in the SEMUCB-WM1 which is present in the other two models and well-constrained by previous waveform modeling effort (e.g., Tan

LAI ET AL. 16 of 19



Acknowledgments

2009935

We thank the editorial team, Jerome

Ritsema, Daniel Frost, and two anon-

ymous reviewers for their constructive

feedback. The project is supported by

grant NSF-CSEDI-EAR-1161046 and

& Helmberger, 2007). The multiple ScS can potentially be a powerful method but the accuracy of upper mantle structure which is a key reflection point needs to be considered.

5. Conclusions

In this study, we modeled the multipathing of Sdiff and rapid variation of differential ScS-S travel time and proposed a ULVZ-slab interaction at the northeastern edge of the Pacific LLSVP, ~12° southeast of present-day Hawaii. Using published results from mineral physics and geodynamic simulations, we constructed a mineralogical model that accounts for the trade-off between the ULVZ velocity reduction and thickness, and quantitatively explains the observed ULVZ properties with a solid-state assemblage containing iron-rich (Mg, Fe)O magnesio-wüstite. The configuration of the ULVZ and slab is geodynamically favorable for plume triggering and fits the location of the Hawaiian plume root proposed by mantle flow models that can explain many defining features of Hawaii-Emperor Seamount chain.

Data Availability Statement

Waveform data from USArray (https://doi.org/10.7914/SN/TA) were obtained through Incorporated Research Institutions for Seismology (IRIS). Several plots were made using the Generic Mapping Tools version 4.2.1 (Wessel & Smith, 1998).

References

Berryman, J. G. (2000). Seismic velocity decrement ratios for regions of partial melt in the lower mantle. *Geophysical Research Letters*, 27(3), 421–424. https://doi.org/10.1029/1999gl008402

Best, W. J., Johnson, L. R., & McEvilly, T. V. (1974). ScS and mantle beneath Hawaii. *Transactions-American Geophysical Union*, 55(12), 1147. Bower, D. J., Wicks, J. K., Gurnis, M., & Jackson, J. M. (2011). A geodynamic and mineral physics model of a solid-state ultralow-velocity zone. *Earth and Planetary Science Letters*, 303(3–4), 193–202. https://doi.org/10.1016/j.epsl.2010.12.035

Burke, K., & Torsvik, T. H. (2004). Derivation of large igneous provinces of the past 200 million years from long-term heterogeneities in the deep mantle. Earth and Planetary Science Letters, 227(3–4), 531–538. https://doi.org/10.1016/j.epsl.2004.09.015

Chandler, B., Bernier, J., Diamond, M., Kunz, M., & Wenk, H. R. (2021). Exploring microstructures in lower mantle mineral assemblages with synchrotron x-rays. *Science Advances*, 7(1), eabd3614. https://doi.org/10.1126/sciadv.abd3614

Cottaar, S., & Romanowicz, B. (2012). An unusually large ULVZ at the base of the mantle near Hawaii. Earth and Planetary Science Letters, 355, 213–222. https://doi.org/10.1016/j.epsl.2012.09.005

Dannberg, J., Myhill, R., Gassmöller, R., & Cottaar, S. (2021). The morphology, evolution and seismic visibility of partial melt at the core–mantle boundary: Implications for ULVZs. *Geophysical Journal International*, 227(2), 1028–1059.

Dobrosavljevic, V. V., Sturhahn, W., & Jackson, J. M. (2019). Evaluating the role of iron-rich (Mg, Fe)O in ultralow velocity zones. *Minerals*, 9, 762. https://doi.org/10.3390/min9120762

Finkelstein, G. J., Jackson, J. M., Said, A., Alatas, A., Leu, B. M., Sturhahn, W., & Toellner, T. S. (2018). Strongly anisotropic magnesiowüstite in Earth's lower mantle. *Journal of Geophysical Research: Solid Earth, 123*(6), 4740–4750. https://doi.org/10.1029/2017jb015349

Fouch, M. J., Fischer, K. M., & Wysession, M. E. (2001). Lowermost mantle anisotropy beneath the Pacific: Imaging the source of the Hawaiian plume. Earth and Planetary Science Letters, 190(3–4), 167–180. https://doi.org/10.1016/s0012-821x(01)00380-6

French, S. W., & Romanowicz, B. A. (2014). Whole-mantle radially anisotropic shear velocity structure from spectral-element waveform tomography. *Geophysical Journal International*, 199(3), 1303–1327. https://doi.org/10.1093/gjj/ggu334

French, S. W., & Romanowicz, B. A. (2015). Broad plumes rooted at the base of the Earth's mantle beneath major hotspots. *Nature*, 525(7567), 95. https://doi.org/10.1038/nature14876

Frost, D. A., & Rost, S. (2014). The P-wave boundary of the large-low shear velocity province beneath the Pacific. *Earth and Planetary Science Letters*, 403, 380–392. https://doi.org/10.1016/j.epsl.2014.06.046

Grand, S. P., & Helmberger, D. V. (1984). Upper mantle shear structure of North America. *Geophysical Journal International*, 76(2), 399–438.

https://doi.org/10.1111/j.1365-246x.1984.tb05053.x
Hassan, R., Müller, R. D., Gurnis, M., Williams, S. E., & Flament, N. (2016). A rapid burst in hotspot motion through the interaction of tectonics

and deep mantle flow. *Nature*, 533(7602), 239–242. https://doi.org/10.1038/nature17422

He, Y., & Wen, L. (2012). Geographic boundary of the "Pacific Anomaly" and its geometry and transitional structure in the north. *Journal of*

Geophysical Research: Solid Earth, 117(B9), B09308. https://doi.org/10.1029/2012jb009436

Hu, J., Gurnis, M., Rudi, J., Stadler, G., & Müller, D. (2022). Dynamics of abrupt change in Pacific Plate motion around 50 Ma. Nature Geosci-

ence, 15, 74–78. https://doi.org/10.1038/s41561-021-00862-6
IRIS Transportable Array. (2003). USArray Transportable Array. International Federation of Digital Seismograph Networks. https://doi.

org/10.7914/SN/TA

Jackson, J. M., & Thomas, C. (2021). Seismic and mineral physics constraints on the D' layer. In H. Marquardt, M. Ballmer, S. Cottaar, & J. Konter (Eds.), Mantle convection and surface expressions. Wiley.

Jellinek, A. M., & Manga, M. (2004). Links between long-lived hot spots, mantle plumes, D'', and plate tectonics. *Reviews of Geophysics*, 42(3). https://doi.org/10.1029/2003rs000144

Jenkins, J., Mousavi, S., Li, Z., & Cottaar, S. (2021). A high-resolution map of Hawaiian ULVZ morphology from ScS phases. Earth and Planetary Science Letters, 563, 116885. https://doi.org/10.1016/j.epsl.2021.116885

Julian, B. R. (2005). What can seismology say about hotspots. In G. R. Foulger, J. H. Natland, D. C. Presnall, & D. L. Anderson (Eds.), *Plates, plumes and paradigms* (Vol. 388, p. 155). Special Papers-Geological Society of America. https://doi.org/10.1130/0-8137-2388-4.155

LAI ET AL.



- Kanamori, H., & Rivera, L. (2015). Near-vertical multiple ScS phases and vertically averaged mantle properties. *The Interdisciplinary Earth: A Volume in Honor of Don L. Anderson*, 71, 9–31.
- Kennett, B. L. N., & Engdahl, E. R. (1991). Travel times for global earthquake location and phase identification. Geophysical Journal International, 105(2), 429–465. https://doi.org/10.1111/j.1365-246x.1991.tb06724.x
- Komatitsch, D., & Tromp, J. (2002). Spectral-element simulations of global seismic wave propagation—I. Validation. *Geophysical Journal International*, 149(2), 390–412. https://doi.org/10.1046/j.1365-246x.2002.01653.x
- Labrosse, S., Hernlund, J. W., & Coltice, N. (2007). A crystallizing dense magma ocean at the base of the Earth's mantle. *Nature*, 450(7171), 866–869. https://doi.org/10.1038/nature06355
- Lay, T., Hernlund, J., Garnero, E. J., & Thorne, M. S. (2006). A post-perovskite lens and D'' heat flux beneath the central Pacific. *Science*, 314(5803), 1272–1276. https://doi.org/10.1126/science.1133280
- Li, D., Helmberger, D., Clayton, R. W., & Sun, D. (2014). Global synthetic seismograms using a 2-D finite-difference method. Geophysical Journal International, 197(2), 1166–1183. https://doi.org/10.1093/gji/ggu050
- Li, D., Sun, D., & Helmberger, D. (2014). Notes on the variability of reflected inner core phases. Earthquake Science, 27(4), 441–468. https://doi.org/10.1007/s11589-014-0093-9
- Li, M., McNamara, A. K., Garnero, E. J., & Yu, S. (2017). Compositionally-distinct ultra-low velocity zones on Earth's core-mantle boundary. Nature Communications, 8(1), 177. https://doi.org/10.1038/s41467-017-00219-x
- Li, M., & Zhong, S. (2017). The source location of mantle plumes from 3D spherical models of mantle convection. *Earth and Planetary Science Letters*, 478, 47–57, https://doi.org/10.1016/j.epsl.2017.08.033
- Liu, J., Li, J., Hrubiak, R., & Smith, J. S. (2016). Origins of ultralow velocity zones through slab-derived metallic melt. Proceedings of the National Academy of Sciences, 113(20), 5547–5551. https://doi.org/10.1073/pnas.1519540113
- Lyubetskaya, T., & Korenaga, J. (2007). Chemical composition of Earth's primitive mantle and its variance: 1. Method and results. *Journal of Geophysical Research*, 112(B3), B03211. https://doi.org/10.1029/2005jb004223
- Maguire, R., Ritsema, J., van Keken, P. E., Fichtner, A., & Goes, S. (2016). P-and S-wave delays caused by thermal plumes. Geophysical Journal International. 206(2), 1169–1178. https://doi.org/10.1093/gij/ggw187
- Mavko, G., Mukerji, T., & Dvorkin, J. (2010). The rock physics handbook. Cambridge university press.
- Montelli, R., Nolet, G., Dahlen, F. A., & Masters, G. (2006). A catalogue of deep mantle plumes: New results from finite-frequency tomography. *Geochemistry, Geophysics, Geosystems*, 7(11), Q1100. https://doi.org/10.1029/2006gc001248
- Moulik, P., & Ekström, G. (2014). An anisotropic shear velocity model of the Earth's mantle using normal modes, body waves, surface waves and long-period wave- forms. Geophysical Journal International, 199(3), 1713–1738. https://doi.org/10.1093/gji/ggu356
- Nelson, P. L., & Grand, S. P. (2018). Lower-mantle plume beneath the Yellowstone hotspot revealed by core waves. *Nature Geoscience*, 11(4), 280–284. https://doi.org/10.1038/s41561-018-0075-y
- Ni, S., Helmberger, V. D., & Tromp, J. (2005). Three-dimensional structure of the African superplume from waveform modelling. *Geophysical Journal International*, 161(2), 283–294. https://doi.org/10.1111/j.1365-246x.2005.02508.x
- Ohta, K., Fujino, K., Kuwayama, Y., Kondo, T., Shimizu, K., & Ohishi, Y. (2014). Highly conductive iron-rich (Mg, Fe) O magnesiowüstite and its stability in the Earth's lower mantle. *Journal of Geophysical Research: Solid Earth*, 119(6), 4656–4665. https://doi.org/10.1002/2014jb010972
- Pradhan, G. K., Fiquet, G., Siebert, J., Auzende, A.-L., Morard, G., Antonangeli, D., & Garbarino, G. (2015). Melting of MORB at core-mantle boundary. Earth and Planetary Science Letters, 431, 247–255. https://doi.org/10.1016/j.epsl.2015.09.034
- Reali, R., Jackson, J. M., Van Orman, J., Bower, D. J., Carrez, P., & Cordier, P. (2019). Modeling viscosity of (Mg, Fe) O at lowermost mantle conditions. *Physics of the Earth and Planetary Interiors*, 287, 65–75. https://doi.org/10.1016/j.pepi.2018.12.005
- Reiss, M. C., Long, M. D., & Creasy, N. (2019). Lowermost mantle anisotropy beneath Africa from differential SKS-SKKS shear-wave splitting. Journal of Geophysical Research: Solid Earth, 124(8), 8540–8564. https://doi.org/10.1029/2018jb017160
- Ritsema, J., Deuss, A., Van Heijst, H. J., & Woodhouse, J. H. (2011). S40RTS: A degree-40 shear-velocity model for the mantle from new Rayleigh wave dispersion, teleseismic traveltime and normal-mode splitting function measurements. *Geophysical Journal International*, 184(3), 1223–1236. https://doi.org/10.1111/j.1365-246x.2010.04884.x
- Simmons, N. A., Forte, A. M., Boschi, L., & Grand, S. P. (2010). GyPSuM: A joint tomographic model of mantle density and seismic wave speeds. *Journal of Geophysical Research*, 115(B12), B12310. https://doi.org/10.1029/2010jb007631
- Steinberger, B., Sutherland, R., & O'connell, R. J. (2004). Prediction of Emperor-Hawaii seamount locations from a revised model of global plate motion and mantle flow. *Nature*, 430(6996), 167–173. https://doi.org/10.1038/nature02660
- Sun, D., Helmberger, D., Lai, V. H., Gurnis, M., Jackson, J. M., & Yang, H.-Y. (2019). Slab control on the northeastern edge of the mid-Pacific LLSVP near Hawaii. *Geophysical Research Letters*, 46(6), 3142–3152. https://doi.org/10.1029/2018g1081130
- Sun, D., Helmberger, D., Ni, S., & Bower, D. (2009). Direct measures of lateral velocity variation in the deep Earth. *Journal of Geophysical Research*, 114(B5), B05303. https://doi.org/10.1029/2008jb005873
- Tan, E., Leng, W., Zhong, S., & Gurnis, M. (2011). On the location and mobility of thermo-chemical structures with high bulk modulus in the 3-D compressible mantle. Geochemistry, Geophysics, Geosystems, 12, Q07005. https://doi.org/10.1029/2011GC003665
- Tan, Y., & Helmberger, D. V. (2007). Trans-Pacific upper mantle shear velocity structure. *Journal of Geophysical Research*, 112(B8), B08301.
- https://doi.org/10.1029/2006jb004853

 Tarduno, J., Bunge, H.-P., Sleep, N., & Hansen, U. (2009). The bent Hawaiian-Emperor hotspot track: Inheriting the mantle wind. *Science*, 324(5923), 50–53. https://doi.org/10.1126/science.1161256
- Thorne, M. S., & Garnero, E. J. (2004). Inferences on ultra low-velocity zone structure from a global analysis of SPdKS waves. *Journal of Geophysical Research*, 109(B8), B08301. https://doi.org/10.1029/2004jb003010
- Thorne, M. S., Takeuchi, N., & Shiomi, K. (2019). Melting at the edge of a slab in the deepest mantle. *Geophysical Research Letters*, 46(14),
- 8000-8008. https://doi.org/10.1029/2019gl082493

 To, A., Fukao, Y., & Tsuboi, S. (2011). Evidence for a thick and localized ultra low shear velocity zone at the base of the mantle beneath the

central Pacific. Physics of the Earth and Planetary Interiors, 184(3-4), 119-133. https://doi.org/10.1016/j.pepi.2010.10.015

- Torsvik, T. H., Burke, K., Steinberger, B., Webb, S. J., & Ashwal, L. D. (2010). Diamonds sampled by plumes from the core–mantle boundary. Nature, 466(7304), 352–355. https://doi.org/10.1038/nature09216
- Watt, J. P., Davies, G. F., & O'Connell, R. J. (1976). The elastic properties of composite materials. *Reviews of Geophysics*, 14(4), 541–563. https://
- doi.org/10.1029/rg014i004p00541
 Wessel, P., & Smith, W. H. F. (1998). New, improved version of generic mapping tools released. EOS Trans. AGU, 79(47), 579. https://doi.org/10.1029/98EO00426
- Wicks, J. K., Jackson, J. M., Sturhahn, W., & Zhang, D. (2017). Sound velocity and density of magnesiowüstites: Implications for ultralow-velocity zone topography. *Geophysical Research Letters*, 44(5), 2148–2158. https://doi.org/10.1002/2016gl071225

LAI ET AL. 18 of 19



Yu, S., & Garnero, E. J. (2018). Ultralow velocity zone locations: A global assessment. Geochemistry, Geophysics, Geosystems, 19(2), 396–414. https://doi.org/10.1002/2017gc007281

Zhao, C., Garnero, E. J., Li, M., McNamara, A., & Yu, S. (2017). Intermittent and lateral varying ULVZ structure at the northeastern margin of the Pacific LLSVP. *Journal of Geophysical Research: Solid Earth*, 122(2), 1198–1220. https://doi.org/10.1002/2016jb013449

Zhao, D. (2004). Global tomographic images of mantle plumes and subducting slabs: Insight into deep earth dynamics. *Physics of the Earth and Planetary Interiors*, 146(1–2), 3–34. https://doi.org/10.1016/j.pepi.2003.07.032

References From the Supporting Information

Dorfman, S. M., Nabiei, F., Boukaré, C. E., Prakapenka, V. B., Cantoni, M., Badro, J., & Gillet, P. (2021). Composition and pressure effects on partitioning of ferrous iron in iron-rich lower mantle heterogeneities. *Minerals*, 11(5), 512.

Hosseini, K., Matthews, K. J., Sigloch, K., Shephard, G. E., Domeier, M., & Tsekhmistrenko, M. (2018). Submachine: Web-based tools for exploring seismic tomography and other models of Earth's deep interior. *Geochemistry, Geophysics, Geosystems*, 19(5), 1464–1483.

Shukla, G., Wu, Z., Hsu, H., Floris, A., Cococcioni, M., & Wentzcovitch, R. M. (2015). Thermoelasticity of Fe²⁺-bearing bridgmanite. *Geophysical Research Letters*, 42(6), 1741–1749.

Tange, Y., Takahashi, E., Nishihara, Y., Funakoshi, K. I., & Sata, N. (2009). Phase relations in the system MgO-FeO-SiO₂ to 50 GPa and 2000 C: An application of experimental techniques using multianvil apparatus with sintered diamond anvils. *Journal of Geophysical Research*, 114(B2), B02214. https://doi.org/10.1029/2008JB005891

LAI ET AL. 19 of 19